Chemical Engineering Journal 343 (2018) 572–582

Contents lists available at ScienceDirect

Chemical Engineering Journal

journal homepage: www.elsevier.com/locate/cej

Porous Co_3S_4@Ni_3S_4 heterostructure arrays electrode with vertical electrons and ions channels for efficient hybrid supercapacitor

Zhiyong Gao[a], Chen Chen[a], Jiuli Chang[a,*], Liming Chen[a], Panyue Wang[a], Dapeng Wu[a,*], Fang Xu[a], Kai Jiang[b,*]

[a] School of Chemistry and Chemical Engineering, Henan Key Laboratory of Boron Chemistry and Advanced Energy Materials, Henan Normal University, Henan Xinxiang 453007, PR China
[b] School of Environment, Henan Normal University, Henan Xinxiang 453007, PR China

HIGHLIGHTS

- Core shell hierarchical arrays with high electrons and ions mobilities were prepared.
- High faradic activity, decent rate capability and cycleability were yielded.
- High areal energy and power densities were delivered by the hybrid supercapacitor.

GRAPHICAL ABSTRACT

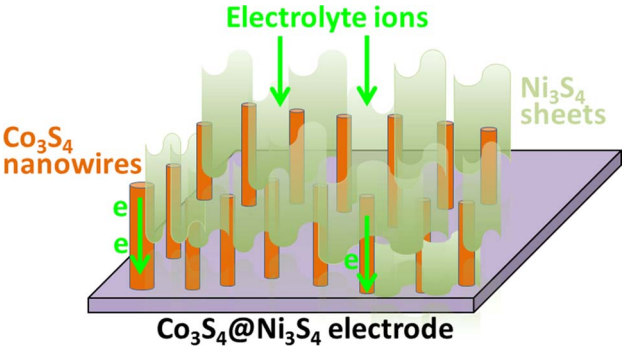

ARTICLE INFO

Keywords:
Core-sheath structure
Sulfide
Faradic
Asymmetric supercapacitor
Areal capacitance

ABSTRACT

Faradic electrodes with large specific surface areas, efficient electrons/ions migration channels and high redox activities are essential prerequisites for high performance supercapacitors. Herein, highly porous Co_3S_4@Ni_3S_4 heterostructure arrays were prepared onto Ni foam substrate by a facile two-step hydrothermal route for application as supercapacitor electrode. Because of the novel core-sheath heterostructure with vertically aligned porous nanowires arrays and macroporous channels, the Co_3S_4@Ni_3S_4 electrode can offer high electrons/ions mobilities and large specific surface area, therefore enables an areal capacitance (C_A) of 3.6 F cm^{-1} at 0.8 mA cm^{-2} and 80% initial C_A maintaining ratio undergoes 5000 consecutive charge-discharge cycles. When used as positive electrode of hybrid supercapacitor, the lightweight Co_3S_4@Ni_3S_4//porous carbon hybrid supercapacitor delivers an areal capacitance of 0.513 F cm^{-2} at 2 mA cm^{-2} and moderate rate capability, therefore can deliver areal energy densities of 0.19–0.021 mWh cm^{-2} within areal power density range of 1.72–38.4 mW cm^{-2}, good cycleability and slow self-discharge behavior. The current Co_3S_4@Ni_3S_4 heterostructure arrays electrode paves a feasible avenue to improve the capacitive performances of supercapacitors through construction of hierarchically porous nanoarrays architectures.

* Corresponding authors.
E-mail addresses: jiulichang@163.com (J. Chang), dapengwu@163.com (D. Wu), kjiang512@163.com (K. Jiang).

https://doi.org/10.1016/j.cej.2018.03.042
Received 17 January 2018; Received in revised form 6 March 2018; Accepted 8 March 2018
Available online 09 March 2018
1385-8947/

1. Introduction

Supercapacitors represent a significant type of rechargeable energy devices with irreplaceable merits such as high power density, fast charging/discharging rate, long cycling life and superior operation safety [1,2], therefore can be widely applied in hybrid electric vehicles, portable electronic devices and backup energy systems [3]. According to charge storage rationale, supercapacitors can be categorized into electric double layered (EDL-) capacitor and faradic capacitor, of which the EDL-supercapacitor operates through the fast electrostatic adsorption of counter ions at porous electrode surface under external electric fields, therefore features high power density. In contrast, the faradic capacitor fulfills charge storage through the redox reaction of active electrode [4–6]. Obviously, mainly due to the battery like charge storage mechanism, the specific capacitance of faradic capacitor is substantially higher over EDL-counterpart. Hence, the faradic metallic oxides or sulfides electrode materials have attracted widespread concerns for the potential to overcome the shortage in energy density of supercapacitor. However, the redox kinetics of faradic material is normally much slower than the EDL-material, which inevitably reduces the power density. To overcome this dilemma, hybrid supercapacitor (HSC), composing of a faradic electrode and an EDL-electrode is ever-booming for the feasibility to balance the energy and power delivery abilities. In term of HSC, the enhancement in specific capacitances of both faradic and EDL-electrodes is a fundamental way to further maximize the energy density. In this sense, the improvement in specific capacitance of individual electrode by rational structure and component design is currently the major target in supercapacitor domain.

As for faradic electrode materials, the transitional metal sulfides are especially intriguing for the intrinsically high redox activities relative to the metallic oxides analogs [7,8], as well as the higher conductivities as a consequence of the lower optical band gap energy [9]. Recent achievements have shown that the heterostructure composing of different sulfides can offer dramatically improved capacitive performances through the combined and even synergistic effect of different components. Additionally, the electrons/ions migration paths can be optimized through the construction of vertically aligned sulfides heterostructure arrays [10–12], so that the sufficient exposure of surface active sites and further the maximized capacitive performances can be offered. To this end, sulfides heterostructures with different architectures, including nanorod/nanowire arrays [12,13], hierarchical arrays [14–17] and nanosheet arrays [18,19] have attracted great investigation enthusiasm, and ideal capacitive performances were harvested. As a typical example, Yuan et al. designed hetero-Ni_7S_6/Co_3S_4 hollow nanoboxes by anions exchange sulfidation using carbonates as self-sacrificing template and precursor, high faradic capacitance and further competitive energy density of the resultant asymmetric supercapacitor can be harvested [20]. Moreover, the direct deposition of active material onto current collector avoids the utilization of binders and conductive additives that hinder the exposure of active material, therefore can maximize the capacitive performance to the uttermost. Following this consideration, Zhai and coworkers [21] reported the preparation of Ni_3S_2/$CoNi_2S_4$ heterostructure arrays, efficient electrons/ions mobilities were guaranteed by constructing architecture with porous channels, therefore enabled pronounced faradic reaction and maximized capacitive performance. Li et al. employed in situ oxidation to prepare $Cu(OH)_2$ nanowires array onto Cu foam substrate, followed by hydrothermal depositing of a layer of $Ni_2(OH)_2CO_3$ to afford hierarchical nanowire array, the apparently increased specific surface area and electrons/ions diffusion rates substantially enhanced the capacitive performances [22]. Chu et al. [10] employed electrodeposition technique to coat nickel sulfide shell layer on the hydrothermally grown $NiCo_2O_4$ nanosheets array to afford hierarchical core-shell electrode, high areal capacitance were successfully yielded. All these works verify the feasibility to substantially improve the capacitive performances of faradic electrodes *via* hierarchical arrays.

Based on the above considerations, herein, Co_3S_4@Ni_3S_4 heterostructure arrays with hierarchically porous texture were directly grown onto Ni foam substrate through a two-step hydrothermal route. The initially deposited Co precursor nanowire arrays not only act as Co source toward porous Co_3S_4 nanowire arrays, but serve as backbones for the construction of Ni_3S_4 nanosheets network with vertical macroporous channels. On the other hand, the intertwined Ni_3S_4 nanosheets network not only provides rich redox sites, but constructs effective conductive channels. As a result, the Co_3S_4@Ni_3S_4 heterostructure electrode can offer high areal capacitance (C_A), decent rate capability and good cycleability. When used as positive electrode of HSC, the Co_3S_4@Ni_3S_4//porous carbon supercapacitor delivers considerable areal energy density and good cycleablity, highlighting the potential of the Co_3S_4@Ni_3S_4 heterostructure arrays as competitive electrode material in high performance and long lifetime energy storage device.

2. Experimental

2.1. Preparation of Co precursor nanowire arrays electrode

All chemicals were of analytical grade and used as received. A piece of Ni foam (1.5 × 1.5 × 0.1 cm^3) was initially rinsed with 0.1 M HNO_3 for 0.5 h to remove the oxides and impurities, followed by washing thoroughly with deionized (DI) water and ethanol. The Co precursor nanowire arrays electrode was prepared by hydrothermal reaction. In brief, 5 mmol of cobalt nitrate was dissolved in 60 mL DI water, followed by addition of 30 mmol urea under vigorous stirring for 2 h to form a clear reaction mixture. The reaction mixture was then transferred to a 100 mL Teflon-lined stainless steel autoclave, and the clean Ni foam substrate was slantly immersed in the reaction solution. Thereafter, the autoclave was sealed and heated at 120 °C for 12 h to hydrothermally depositing the Co precursor onto Ni foam substrate. After being cooled down to room temperature, the active material loaded Ni foam was ultrasonically rinsed with DI water to eliminate the redundant section and dried at 60 °C, thus afforded Co precursor electrode.

2.2. Preparation of Co_3S_4@Ni_3S_4 electrode

Porous Co_3S_4@Ni_3S_4 heterostructure electrode was prepared by immersing the Co precursor loaded Ni foam substrate in a 50 mL autoclave containing 40 mL of 0.05 M aqueous Na_2S solution, the autoclave was then heated at 120 °C for 6 h. After being cooled, rinsed with DI water and vacuumly dried at 60 °C for 24 h, the afforded electrode was labeled as Co_3S_4@Ni_3S_4 electrode. In controlled experiments, different Na_2S concentrations (0.1 and 0.2 M) were also used to prepare Co_3S_4@Ni_3S_4 electrodes, which were denoted as Co_3S_4@Ni_3S_4-0.1 and Co_3S_4@Ni_3S_4-0.2 electrodes according to the concentration of Na_2S. The electrodes were also prepared with the same Na_2S concentration (0.05 M) whereas longer hydrothermal durations (12 and 24 h), which were denoted as Co_3S_4@Ni_3S_4-12 h and Co_3S_4@Ni_3S_4-24 h. As a comparison, mere Ni_3S_4 electrode was also prepared by directly hydrothermal sulfidation of bare Ni foam substrate in 0.05 M Na_2S solution at 120 °C for 6 h.

2.3. The fabrication of carbon ink derived porous carbon electrode

The porous carbon (PC) electrode was prepared by carbon ink impregnation and followed pyrolysis treatment. Concretely, a piece of clean Ni foam substrate (1.5 × 1.5 × 0.1 cm^3) was directly immersed into 10 mL carbon ink (Hero brand) for 10 min under ultrasonication and then dried overnight at 60 °C to complete a cycle of impregnation. The impregnation process could be performed repeatedly to increase the loading amount of carbon ink as needed. Thereafter, the carbon ink loaded Ni foam was pyrolyzed at 300 °C in N_2 atmosphere for 2 h to carbonize the surfactant in carbon ink, thus afforded PC electrode.

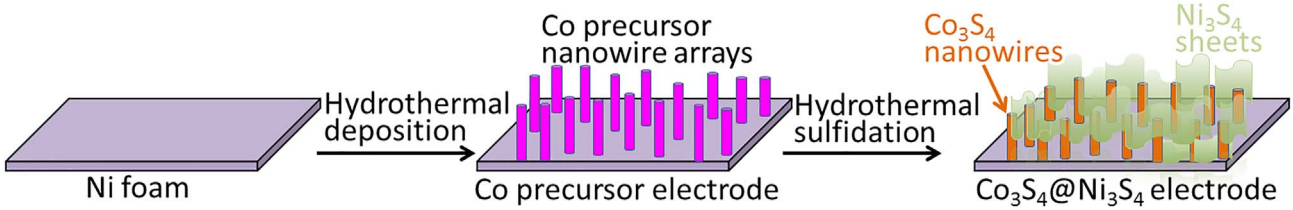

Fig. 1. Schematic illustration on the preparation steps of Co_3S_4@Ni_3S_4 electrode.

2.4. Characterizations

The morphologies and microstructures of the electrode materials were characterized by scanning electrons microscopy (SEM, Hitachi SU-8000 with accelerating voltage of 15 kV) coupled with energy dispersive spectroscopy (EDS) and high resolution transmittance electrons microscopy (TEM, JEOL JEM-2100 with accelerating voltage of 200 kV). The phases, structure and chemical compositions were identified by X-ray powder diffraction (XRD, Bruker D8 diffractometer with Cu Ka radiation, λ = 0.15418 nm), Raman spectroscopy (JOBIN YVON HR800 Confocal Raman spectrometer with 632.8 nm laser excitation) and X-ray photoelectron spectroscopy (XPS, Kratos Amicus X-ray photoelectron spectrometer with Mg Ka radiation under 2×10^{-6} Pa). N_2 sorption isotherms of the electrodes were tested on a Micromeritics ASAP 2020 surface analyzer at 77 K. The specific surface areas (S_{BET}s) were calculated by multiple points Brunauer-Emmett-Teller (BET) method, and the pore size distributions were analyzed from the adsorption branch according to Barrett-Joyner-Halenda (BJH) model.

2.5. Electrochemical measurements

Cyclic voltammograms (CVs), galvanostatic charge-discharges (GCDs) and electrochemical impedance spectra (EISs) of the electrodes were measured on CHI 660D work station (Shanghai Chenhua) in 3-electrode configuration. The half-cell comprises an active material deposited Ni foam working electrode, a HgO/Hg reference electrode and a platinum foil auxiliary electrode immersed in 2 M KOH electrolyte. CVs were recorded in potential scan rate range of 1–100 mV s^{-1}. EISs were recorded over $10^5 \sim 0.01$ Hz with an ac perturbation of 5 mV. The areal capacitances (C_As) of the electrodes were calculated based on the discharge time in GCD according to Eq. (1) [7]:

$$C_A = It/sV \quad (1)$$

where I (A) represents discharge current, V (V) is the potential window of the half-cell, t (s) stands for the discharge time, s (cm^2) is the geometric area of working electrode.

In the case of HSC, the Co_3S_4@Ni_3S_4 electrode and PC electrode were used as positive and negative electrodes, respectively, which were face-to-face assembled with a cellulose paper sandwiched between them to afford 2-electrode full-cell immersed in 2 M KOH electrolyte. The mass of PC onto negative electrode was optimized to be 3 mg through a series of trials. GCDs of the HSC were measured on a Lanhe CT2001A cell test system (Wuhan China). The areal capacitance of the HSC (C_{cell}) was also calculated based on Eq. (1), but the variate V herein is the total voltage window of the full-cell, and s (cm^2) represents the geometric area of the HSC. The areal energy density (E_A, mWh cm^{-2}) and power density (P_A, mW cm^{-2}) were calculated based on $E_A = \int IV(t)dt/3.6$ and $P_A = 3600E_A/t$ [23], and the volumetric energy density (E_V), power density (P_V) were calculated according to $E_V = E_A \times s/v$ and $P_V = P_A \times s/v$, v (cm^3) herein is the geometric volume of HSC.

3. Results and discussion

3.1. Structural characterizations of Co_3S_4@ Ni_3S_4 electrodes

Co_3S_4 and Ni_3S_4 are traditional faradic materials that store charges through the redox reactions of Co and Ni elements, the heterostructures based on Co_3S_4 (Ni_3S_4) and other sulfides can further optimize the redox activities and therefore the faradic properties [21,24,25]. Considering the high faradic activities of Co_3S_4 and Ni_3S_4, the heterostructure composite based on the two sulfides is deemed to be superior electrode material with further improved capacitive performance [12–17]. Although the capacitive performances of faradic electrodes rely mainly on the intrinsic redox activities of active materials themselves, the tailored architectures of active materials with more exposed surface sites and more efficient electrons/ions migration channels can further maximize the capacitive performances. Low dimensional nanowire arrays and hierarchically porous architecture with vertical porous channels can offer efficient electrons/ions mobilities with short path length and enlarged accessible surface areas, hence the active materials with nanowires and (or) hierarchically porous architectures are ideal selections for faradic electrodes. Moreover, the binder and conductive additive free faradic electrode by direct deposition of active material onto current collector can effectively increase the surface utilization ratio of active material, therefore enables obviously higher faradic capacitance. Herein, highly porous Co_3S_4@Ni_3S_4 heterostructure arrays were constructed directly onto Ni foam substrate, which can be intuitively illustrated in Fig. 1. Initially, Co precursor nanowire arrays were directly grown onto Ni foam substrate by hydrothermal reaction, the nanowire arrays allow the filling of electrolyte ions into deep zone of electrode active layer, therefore enables high faradic capacitance for the exposure of more active surface to electrolyte. In the followed hydrothermal sulfidation process, S^{2-} ions directly convert the Co precursor (mainly cobalt hydroxide or basic carbonate) to Co_3S_4 nanowire arrays through anions exchange reaction. Simultaneously, Ni_3S_4 nanosheets were formed by oxidative etching and sulfidation of Ni foam in Na_2S media, which coated around and on top of the Co_3S_4 nanowires to form the Co_3S_4@Ni_3S_4 heterostructure array electrode. Due to the crystallization habit of Ni_3S_4 generally in sheet configuration, the vertical arrangement and the intertwining of the Ni_3S_4 nanosheets result in the porous architecture with vertical channels. This type of heterostructure allow the easily infiltration of electrolyte ions across the vertically arranged porous channels to deep inner regions, and the bottom Co_3S_4 nanowire arrays facilitate the fast migration of electrons, therefore maximized capacitive performance can be ensured for the sufficient exposure of both components to electrolyte.

The phases of the Co precursor, mere Ni_3S_4 and the Co_3S_4@Ni_3S_4 electrodes are demonstrated in Fig. 2a, except the strong diffractions belonging to Ni foam substrate (44.6, 51.9, and 76.4°, JCPDS No. 01-1258), the absence of discernable diffraction peaks in Co precursor electrode implies the amorphous nature. In contrast, the Co_3S_4@Ni_3S_4 electrode displays a series of diffractions, thereinto, the five peaks emerge at 31.5, 37.9, 49.7, and 55° are corresponded to (3 1 1), (4 0 0), (5 1 1) and (4 4 0) planes reflection of cubic Ni_3S_4 (JCPDS No. 47-1739) [24,26], which are in good agreement with the mere Ni_3S_4 electrode prepared by directly hydrothermal sulfidation of Ni foam substrate. Because no Ni salt is introduced throughout the preparation process, the formation of Ni_3S_4 is presumably due to the oxidative etching of Ni foam in the presence of the precipitator (S^{2-}) toward oxidized forms of Ni element (Ni^{2+} and Ni^{3+}) during the hydrothermal sulfidation step.

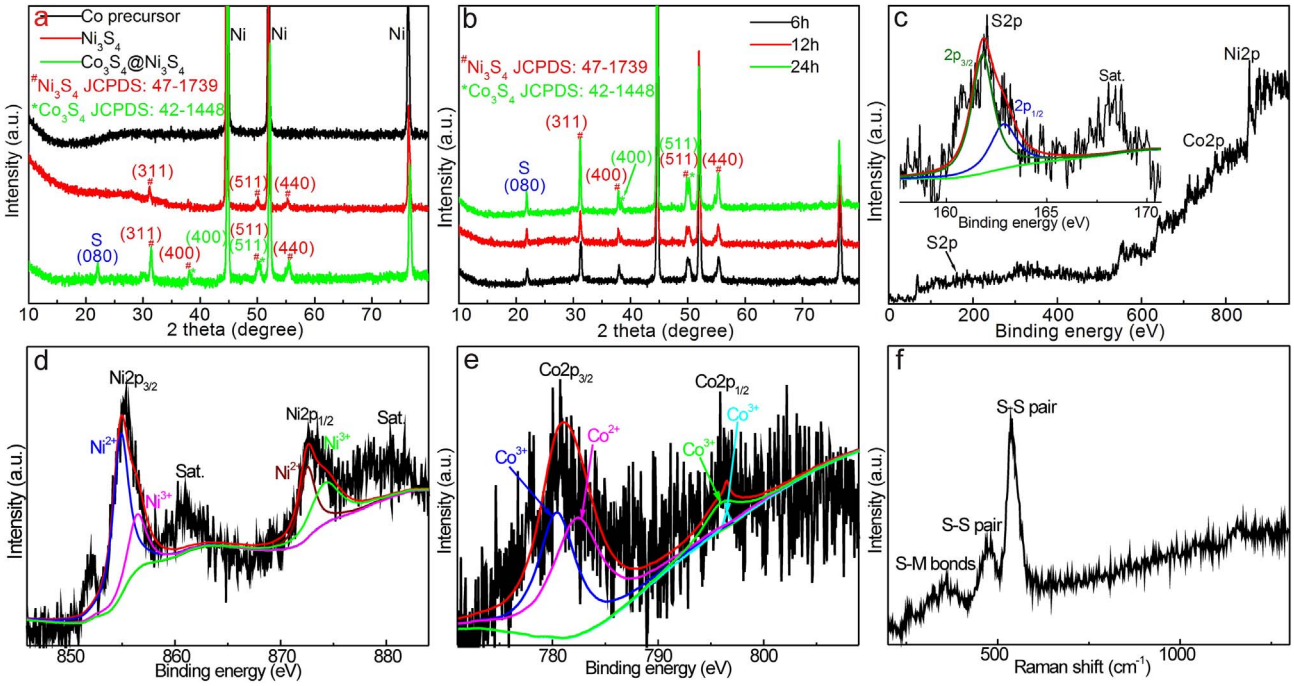

Fig. 2. (a) XRD patterns of Co precursor, Ni_3S_4 and Co_3S_4@Ni_3S_4 electrodes, (b) XRD patterns of Co_3S_4@Ni_3S_4 electrodes prepared at different hydrothermal sulfidation time, (c) XPS survey spectrum and S2p spectrum (inset), (d) Ni2p, (e) Co2p XPS spectra and (f) Raman spectrum of Co_3S_4@Ni_3S_4.

Wang et al. deemed that S^{2-} can etch Ni foam to form NiS following the route: $Na_2S + Ni + H_2O = NiS + 2NaOH + H_2$ [7]. Given the low solubility product (K_{sp}) of nickel sulfides, the S^{2-} can substantially decrease the potential of Ni^{2+}/Ni redox pair and enable the strong reduction ability of Ni, so the formation of NiS and further Ni_3S_4 from metallic Ni are also possible in principle. Besides the diffractions belonging to Ni_3S_4, another two weak but discernable peaks locate at 38.1 and 50.3° are assignable to (4 0 0) and (5 1 1) planes of cubic Co_3S_4 (JCPDS No. 19-0367) [11,27], which indicate the accompanied sulfidation and oxidation of the Co precursor toward Co_3S_4 via anions exchange and redox reactions. Considering the similar (4 0 0) and (5 1 1) planes spacings between Ni_3S_4 and Co_3S_4 from the similar diffraction angles, the good lattice matching facilitates the formation of stable heterostructure between the two sulfides undergoes gradual aging during hydrothermal sulfidation process. Due to the sulfidation of Co precursor occurs within the interior of nanowires, the relatively slower precipitation conversion kinetics causes the insufficient content or the weak crystallinity of Co_3S_4, which results in the weak diffractions indexable to Co_3S_4. Hence, the Co_3S_4@Ni_3S_4 electrodes prepared at longer hydrothermal sulfidation durations were further investigated. As shown in Fig. 2b, the diffraction peaks belonging to both Co_3S_4 and Ni_3S_4 components increase gradually with the hydrothermal sulfidation time, this trend indicates that the longer hydrothermal time not only causes the coating and crystallization of Ni_3S_4 sheath, but causes the aging of the embedded Co_3S_4 core. To be mentioned, the diffraction at 21° is not ascribable to any phases of CoS_x or NiS_x, whereas matches to the (0 8 0) planes of sulfur (24-1251), showing the hydrothermal oxidation of S^{2-}. The effect of S^{2-} concentration on the crystallinity of Co_3S_4@Ni_3S_4 electrode was also investigated by hydrothermal sulfidation at different S^{2-} concentrations. From Fig. S1, the diffraction peaks of both Ni_3S_4 and Co_3S_4 elevate obviously with S^{2-} concentration, this trend indicates that the higher S^{2-} concentration also facilitates the faster formation of Co_3S_4@Ni_3S_4 active layer for dynamic factor.

The chemical state of the Co_3S_4@Ni_3S_4 heterostructure composite electrode is identified by XPS. From Fig. 2c, the survey spectrum comprises three peaks located at 164.1, 781.0, and 856.3 eV, which are assignable to the binding energy of S2p, Co2p, and Ni2p orbits, respectively. The absence of O1s peak suggests the complete sulfidation of Co precursor and the formation of Ni_3S_4 sheath. The detailed oxidation states of each element can be revealed by deconvolution of the high resolution peaks. The S2p spectrum (Inset) includes a main peak located at 162.0 eV and a satellite peak at 168 eV, the former peak can be fitted into two peaks at 161.8 and 163 eV, which are ascribable to $S2p_{3/2}$ and $S2p_{1/2}$ orbits of Ni-S and Co-S bonds [25,28–30], evidencing the formation of sulfides in the core-sheath heterostructure composite. The minor satellite peak is presumably due to the partially oxidized surface sulfur species with higher oxidation states [17,30]. The core level Ni2p spectrum (Fig. 2d) mainly comprises two main peaks at 855.4 and 873.3 eV assignable respectively to $Ni2p_{3/2}$ and $Ni2p_{1/2}$ spin orbit doublets and two satellite peaks. By deconvolution of the two main peaks, the $Ni2p_{3/2}$ orbit comprises two peaks with binding energy of 854.6 and 856.5 eV, which are corresponded respectively to the Ni(II) and Ni(III) oxidation states, and the $Ni2p_{1/2}$ orbit can also be fitted into two peaks belonging to Ni(II) (872.3 eV) and Ni(III) (874.5 eV) [31,32], all of these results manifest the coexists of Ni (II) and Ni(III) in the Ni_3S_4 sheath layer. To be mentioned, another weak peak at 852 eV is attributable to Ni(0) of Ni foam substrate beneath the active layer. Because XPS is a surface analysis tool for determining the chemical states of elements with detection depth of only several nanometers, so the weak intensity of this peak is also reasonable. In a similar manner, the $Co2p_{3/2}$ (780.7 eV) and Co $2p_{1/2}$ (796.0 eV) spin orbits can be fitted into Co (III) and Co(II) oxidation states (Fig. 2e), showing the coexistence of Co (III) and Co(II) species in the Co_3S_4 core [11]. The coexistence of +2 and +3 oxidation states in Ni_3S_4 and Co_3S_4 components allow the redox conversions under outer electric fields, the combined redox reactions of both elements guarantee high faradic activity and therefore superior capacitive performance of the Co_3S_4@Ni_3S_4 electrode. Fig. 2f shows the Raman spectrum of Co_3S_4@Ni_3S_4, the wide vibration band around 350 cm^{-1} is mainly attributable to the asymmetric bending vibration of tetra S-Ni(Co) bonds [33], besides, the two strong peaks at 476 and 541 cm^{-1} are derived from the A_g S-S pairs in NiS_x and CoS_x, respectively [34]. All of these characteristic vibrations further verify the containing of Co_3S_4 and Ni_3S_4 in the core-sheath heterostructure composite.

The deposition density and interface compatibility between the Co_3S_4@Ni_3S_4 active layer and Ni foam substrate were investigated by

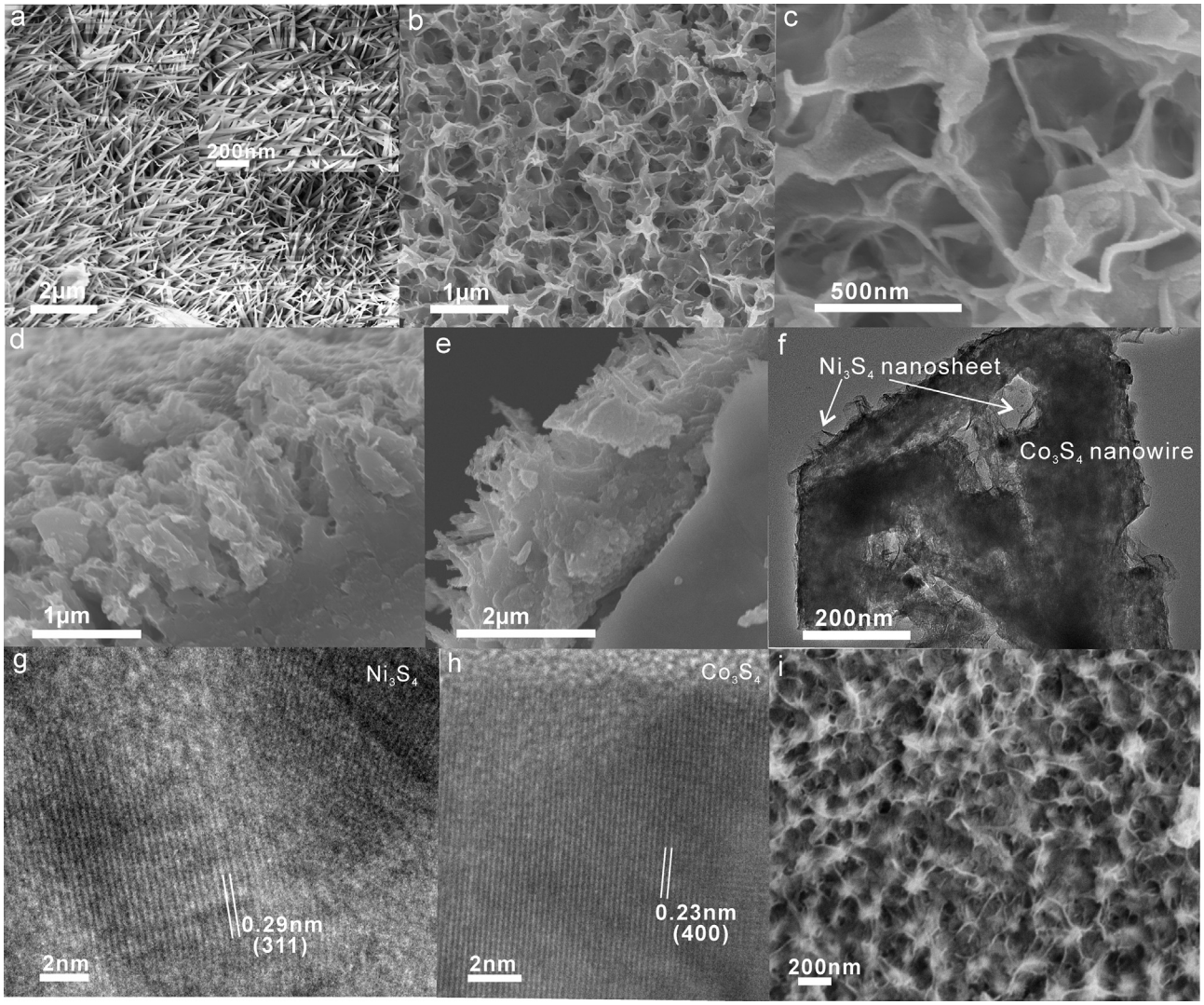

Fig. 3. SEM of (a) Co precursor electrode at different magnifications, (b, c) top-view, (d, e) cross-section of Co_3S_4@Ni_3S_4 electrode at different magnifications and (i) Ni_3S_4 electrode, (f) TEM of Co_3S_4@Ni_3S_4, (g, h) HRTEM of (g) Ni_3S_4 and (h) Co_3S_4 sections.

low magnification SEM and element mapping images, from Fig. S2a, the Co_3S_4@Ni_3S_4 electrode exhibits rough surface with densely coating of activate layer free of apparently detached regions, showing the successful deposition of active layer onto Ni foam substrate with good interface compatibility. The homogeneous distributions of Ni, Co and S elements on the entire surface of Ni foam substrate also indicate the homogeneous coating of Co_3S_4@Ni_3S_4 onto Ni foam substrate (Fig. S2b), which ensures essential conductivity for the Co_3S_4@Ni_3S_4 electrode.

The morphologies and microstructures of the Co precursor, mere Ni_3S_4 and the Co_3S_4@Ni_3S_4 electrodes were characterized by SEM and TEM, from Fig. 3a, the top-view image of the Co precursor electrode demonstrates high density of nanowires with diameter of ca. 100 nm and length of up to 2 μm, which are vertically grown onto Ni foam substrate without peeled regions, showing the good interface compatibility between Co precursor nanowires and Ni foam substrate. Zoom-in image (Inset) reveals the smooth surface and sharp tip of the nanowires, further evidences the easily formation of Co precursor nanowire arrays by hydrolysis of cobalt salt. Undergoes hydrothermal sulfidation treatment, the Co_3S_4@Ni_3S_4 electrode mainly exhibits intertwined nanosheets with vertical macroporous channels (Fig. 3b), which is mainly due to the growth and interconnection of Ni_3S_4 nanosheets onto the simultaneously formed Co_3S_4 nanowire arrays backbone, the overall morphology resembles to graphene aerogel [35]. Closer observation reveals the rough surface of the nanosheets (Fig. 3c), which is constructed by numerous stacked granules. Hence, it can be inferred that the hydrothermal oxidative etching of Ni foam in S^{2-} solution creates rich Ni_3S_4 nucleus, which aggregate onto the Co_3S_4 nanowires to reduce the surface energy arising from the small curvature radius, the further growth and assembly result in intertwined nanosheets network around the nanowire arrays backbone. Meanwhile, the hydrothermal sulfidation and aging cause the anions exchange of Co precursor toward Co_3S_4 nanowire arrays with certain crystallinity, as proved by the diffraction peaks belonging to Co_3S_4 in XRD pattern (Fig. 2a). The cross-section image of Co_3S_4@Ni_3S_4 electrode (Fig. 3d) exhibits vertically arrayed forest with the enwrapping of intertwined thin nanosheets around the nanowire trunks, evidencing the core-sheath structure with the coating and intertwining of Ni_3S_4 nanosheets outside the Co_3S_4 nanowires. In some regions (Fig. 3e), the protruding tips of nanowires can be observed, manifesting the coexistence of Co_3S_4 nanowires in Co_3S_4@Ni_3S_4 electrode. TEM of Co_3S_4@Ni_3S_4 heterostructure composite (Fig. 3f) demonstrates nanowires enwinded by translucent nanosheets, evidences the coating of intertwined ultrathin Ni_3S_4 nanosheets sheath around the Co_3S_4 nanowires core. The alternative dark and light microregions within nanowires indicates the porous texture of the Co_3S_4, which is presumably due to the gradual sulfidation of amorphous Co precursor nanowires from exterior to inner creates numerous Co_3S_4 crystallites, the local variation in atoms stacking density creates rich

inter-crystallite voids. The microstructures of the nanosheets sheath and the nanowire core were characterized by HRTEM, from Fig. 3g, the nanosheet displays discernable lattice fringes with spacing of 0.29 nm, which corresponds to the (3 1 1) planes of cubic Ni_3S_4, evidencing the formation of Ni_3S_4 nanosheets by sulfidation of Ni foam substrate. The nanowire also shows legible lattice fringes with 0.23 nm spacing indexable to (4 0 0) planes of cubic Co_3S_4 (Fig. 3h), manifesting the sulfidation of Co precursor toward Co_3S_4. Based on these characterizations, Co_3S_4@Ni_3S_4 heterostructure with coating of intertwined Ni_3S_4 nanosheets onto the vertically aligned porous Co_3S_4 nanowire arrays was successfully prepared by hydrothermal deposition and sulfidation steps. Without the initially deposited Co precursor nanowire arrays, the mere Ni_3S_4 electrode prepared by hydrothermal sulfidation of Ni foam substrate also demonstrates intertwined nanosheets (Fig. 3i), but the flexible nanosheets incline to collapse and stack to form more dense texture. Based on these morphological comparisons, the Co_3S_4 nanowire arrays is indeed beneficial for the vertical arrangement of Ni_3S_4 nanosheets to form heterostructure arrays with vertical macroporous channels.

In such a core-sheath heterostructure arrays with the coating of porous Ni_3S_4 nanosheets network onto Co_3S_4 nanowire arrays, the Co_3S_4 nanowire arrays not only serve as backbone supporting the intertwined Ni_3S_4 nanosheets porous network without severe collapse and stacking, but increase the conductivity of the active layer by virtue of the vertical conductive channels with short electrons migration distance. Simultaneously, the interconnected Ni_3S_4 nanosheets network with vertical macroporous channels allows the filling of electrolyte into the deep inner zone of the active layer, which increases the utilization ratio of both components. Moreover, the porous texture of Co_3S_4 nanowires and thin Ni_3S_4 nanosheets maximize the accessible inner surface area with short electrolyte diffusion distance, which are beneficial for high capacitive performance. In this sense, the porous Co_3S_4@Ni_3S_4 heterostructure arrays architecture is an ideal selection as faradic electrode.

Fig. 4a shows the N_2 sorption isotherms of the Co precursor, mere Ni_3S_4 and Co_3S_4@Ni_3S_4 electrodes, all of them demonstrate type IV isotherms including a microporous filling at low P/P_0 and a H3 typed hysteresis loop within intermediate and high P/P_0, indicating the coexistence of both micropores and meso-/macropores in the three electrodes [36]. The S_{BET}s of Co precursor, Ni_3S_4 and Co_3S_4@Ni_3S_4 electrodes are 5, 116 and 210 $m^2 g^{-1}$, respectively. The substantially enhanced S_{BET} of the Co_3S_4@Ni_3S_4 electrode is mainly due to the highly porous texture of both components, which offers much more surface sites for faradic reactions, hence a higher faradic capacitance can be ensured. From the BJH pore width distributions shown in Fig. 4b, the Co precursor electrode demonstrates low probabilities within 1–20 nm, showing the limited and inhomogeneous pores within the Co precursor nanowires. In contrast, the Co_3S_4@Ni_3S_4 and mere Ni_3S_4 electrodes demonstrate high probabilities within 10–20 nm, showing the presence of overwhelming mesopores within both components, which agrees with the TEM results (Fig. 3f). Relative to mere Ni_3S_4 electrode, the higher probability of mesopores in Co_3S_4@Ni_3S_4 electrode indicates the higher mesoporosity and therefore larger S_{BET} of the Co_3S_4@Ni_3S_4 electrode, hence high capacitive performance of the Co_3S_4@Ni_3S_4 electrode is imaginable.

3.2. Electrochemical properties of the Co_3S_4@Ni_3S_4 electrode

To assess the capacitive performance of the Co_3S_4@Ni_3S_4 electrode, CVs, GCDs and EISs of the Co_3S_4@Ni_3S_4 electrode, Co precursor electrode and mere Ni_3S_4 electrode were measured and compared. Fig. 5a shows the CVs of the three electrodes at 20 mV s^{-1}, all of them display battery-typed faradic behaviors featured by an anodic capacitive current response and an obvious cathodic peak. The substantially higher redox currents of Co_3S_4@Ni_3S_4 electrode over the other two electrodes indicates the more prominent redox activity, which is mainly associated with the more abundant redox sites as a consequence of the much larger S_{BET}. The redox mechanism of Co_3S_4@Ni_3S_4 electrode in aqueous alkaline solution can be proposed as follows [25,37]:

$$Co_3S_4 + OH^- = Co_3S_4OH^- + e^- \quad (2)$$

$$Co_3S_4OH^- + OH^- = Co_3S_4\ O + H_2\ O + e^- \quad (3)$$

$$Ni_3S_4 + OH^- = Ni_3S_4(OH) + e^- \quad (4)$$

The coupled redox reactions and even the synergy between Co_3S_4 and Ni_3S_4 result in the obviously higher faradic activity of the Co_3S_4@Ni_3S_4 electrode. Mainly due to the similar redox reaction potentials, the superimposition of the multiple redox reactions causes the seemingly only one pair of redox peaks in CV [38]. The obviously higher capacitive property of Co_3S_4@Ni_3S_4 electrode was further proved by GCDs, from Fig. 5b, all of the three electrodes demonstrate obvious faradic potential platforms at charging and discharging stages [39,40]. The negligible inner resistance voltage drops (IRs) manifest the good conductivities of the binder and additives free electrodes. Considering the Ni foam substrate simultaneously serves as current collector and Ni source for Ni_3S_4 sheath, the accurate weights of active materials in Co_3S_4@Ni_3S_4 and mere Ni_3S_4 electrodes are impossible to be accurately measured, so the C_As were employed to express the charge storage capacities. Based on the discharge time, the C_A of Co_3S_4@Ni_3S_4 electrode is 3.6 F cm^{-2} at 0.8 mA cm^{-2}, which is superior to mere Ni_3S_4 electrode (1.17 F cm^{-2} at 0.6 mA cm^{-2}) and Co precursor electrode (2.8 F cm^{-2} at 0.89 mA cm^{-2}). The substantially higher C_A of the Co_3S_4@Ni_3S_4 electrode highlights the potential of the porous Co_3S_4@Ni_3S_4 heterostructure arrays in supercapacitor electrode.

To more in-depth understand the electrochemical kinetics at the faradic electrodes, EISs of the Co_3S_4@Ni_3S_4, mere Ni_3S_4 and Co precursor electrodes were determined in frequency range of 0.01–100 kHz. From Fig. 5c, the Nyquist plots of impedances for all electrodes comprise a low frequency straightline with high slope relative to real axis and an arc at high frequency range, showing the typical faradic feature of all electrodes. Generally, the real axis intercept at high frequency end stands for series resistance (R_s) of electrode, which includes the intrinsic

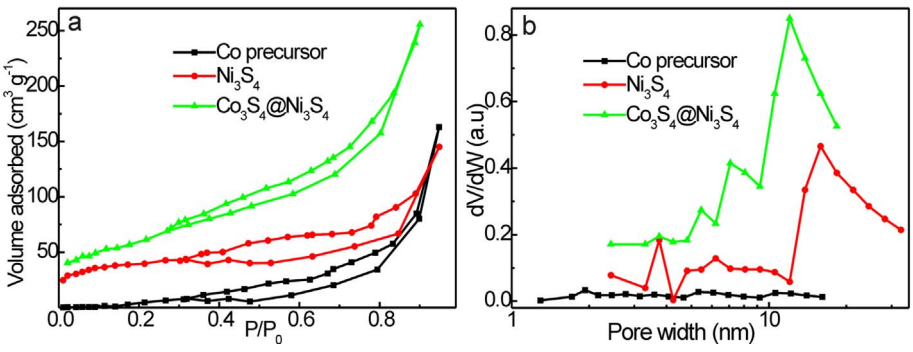

Fig. 4. (a) N_2 sorption isotherms and (b) BJH pore size distributions of the Co precursor, Ni_3S_4 and Co_3S_4@Ni_3S_4.

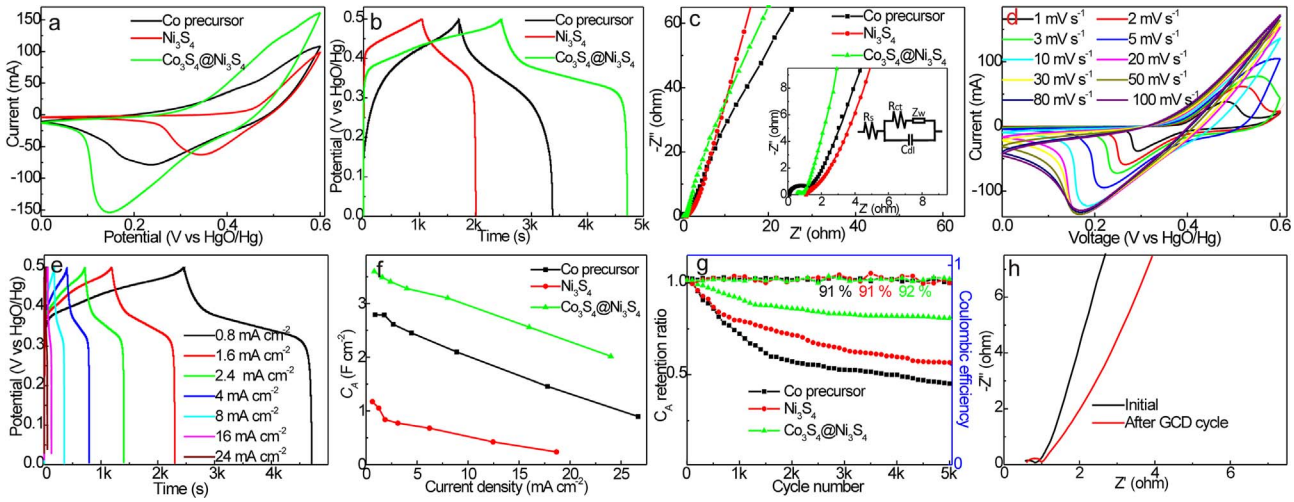

Fig. 5. (a) CVs at 20 mV s^{-1}, (b) GCDs at low current densities, (c) EISs, (f) Rate capabilities and (g) Cycleabilities of Co precursor, mere Ni_3S_4 and Co_3S_4@Ni_3S_4 electrodes. (d) CVs at different potential scan rates and (e) GCDs at various current densities of the Co_3S_4@Ni_3S_4 electrode, (h) EISs of Co_3S_4@Ni_3S_4 electrode before and after 5000 GCD cycles.

resistances of active material, electrolyte and the contact resistance at active material/current collector interface [41]. By fitting the enlarged EISs at high frequency range using the equivalent circuit in inset, the R_ss are 0.5, 0.9, and 0.1 ohm, respectively for Co_3S_4@Ni_3S_4 electrode, mere Ni_3S_4 electrode and Co precursor electrode. Amongst them, the low R_s of the Co precursor electrode is mainly due to the tightly coating of Co precursor nanowire arrays onto Ni foam with good interface compatibility and efficient conductive channels within the nanowire arrays. By sulfidation treatment, the R_s of the Co_3S_4@Ni_3S_4 electrode is apparently lower than the mere Ni_3S_4 electrode, which manifests the crucial contribution of porous Co_3S_4 nanowires to the conductivity of electrode. The arc at high frequency represents the charge transfer resistance (R_{ct}) at electrode/electrolyte interface [41]. The R_{ct}s are 0.5, 0.4 and 1.1 ohm, respectively for Co_3S_4@Ni_3S_4 electrode, mere Ni_3S_4 electrode and Co precursor electrode, the lower R_{ct} values of the former two electrodes reflect the faster redox kinetics for the porous texture with higher S_{BET}s, the exposure of more surface sites to electrolyte are responsible for the more sufficient and rapid faradic reactions and therefore the lower R_{ct}s. The transitional region between the R_{ct} arc and the low frequency straightline reflects the Warburg diffusion resistance of electrolyte ions (Z_w) [42], the Z_ws are negligible for all electrodes (0.04, 0.08 and 0.05 ohm, respectively for Co_3S_4@Ni_3S_4, mere Ni_3S_4 and Co precursor electrodes), showing the facile diffusion of electrolyte into the porous surface in all electrodes. At low frequency region, the slant lines reflect the capacitive behaviors of all electrodes [43,44]. Given the lowest total resistance (the sum of R_s and R_{ct}), the Co_3S_4@Ni_3S_4 electrode is the most preferable faradic electrode. The CVs and GCDs of the Co_3S_4@Ni_3S_4 electrodes prepared at higher S^{2-} concentrations and longer hydrothermal sulfidation durations were also compared (Figs. S3 and S5), the C_A decreases gradually at higher S^{2-} concentration or elongated hydrothermal duration, the over aggregation and crystallization of Ni_3S_4 nanosheets (Figs. S4 and S6) are speculated to be the main reasons for the deteriorated capacitive performances. Based on these comparisons, the typical Co_3S_4@Ni_3S_4 electrode hydrothermally sulfidated at 120 °C for 6 h with S^{2-} concentration of 0.05 M is the optimal electrode in this work.

To more concretely evaluate the capacitive properties of Co_3S_4@Ni_3S_4 electrode, CVs were further measured at various potential scan rates, from Fig. 5d, the cathodic current elevates gradually with scan rate, showing the electrochemical reaction of the electrode is controlled by the redox kinetics of Co_3S_4@Ni_3S_4 active layer and the diffusion of electrolyte. Additionally, the gradual left shift of cathodic potential with scan rate is mainly due to the polarization of electrode for the slow redox kinetics and the relatively insufficient ions diffusion at higher scan rate. To be mentioned, the anodic peak gradually disappears at higher scan rates, suggesting the insufficient oxidation of Co(II) and Ni (II) in sulfides, which will inevitably cause the non-ideal rate capability and cycleability of the electrode. Fig. 5e shows the GCDs of the Co_3S_4@Ni_3S_4 electrode at different areal current densities. From the discharge time, C_As are 3.60, 3.49, 3.41, 3.28, 3.10, 2.56 and 2.02 F cm^{-2}, respectively at 0.8, 1.6, 2.4, 4, 8, 16 and 24 mA cm^{-2}, the 56% C_A retaining ratio within 30 folds enhanced current density verifies the moderate rate capability. To be noted, the C_As values are superior to other sulfides based faradic electrode, such as CuS nanowire arrays electrode (0.38 F cm^{-2} at 2 mA cm^{-2}) [45], nickel sulfide/oxide heterostructure electrode (2.04 F cm^{-2} at 8 mA cm^{-2}) [46], Co_3S_4/NiS nanoplates electrode (1.81 F cm^{-2} at 4 mA cm^{-2}) [7], hierarchical $NiCo_2O_4$@nickel sulfide nanoplate arrays electrode (1.85 F cm^{-2} at 8 mA cm^{-2}) [10], hierarchical $NiCo_2O_4$@Ni_2CoS_4 arrays electrode (1.86 F cm^{-2} at 1 mA cm^{-2}) [16] and vertically aligned Co_3S_4/$CoMo_2S_4$ ultrathin nanosheets on graphene electrode (2.9 F cm^{-2} at 2 mA cm^{-2}) [25] whereas lower than $NiCo_2S_4$@PANI nanowires electrode (4.74 F cm^{-2} at 2 mA cm^{-2}) [13], $Cu_{1-x}Ni_xS$ nanosheets electrode (5.88 F cm^{-2} at 2 mA cm^{-2}) [36] and 3D $ZnCo_2O_4$/$NiMoO_4$ heterostructure electrode (6.07 F cm^{-2} at 2 mA cm^{-2}) [47]. Fig. 5f summaries the rate capabilities of different electrodes within 30 folds enhanced current densities, the C_A retaining ratio of the Co_3S_4@Ni_3S_4 electrode is apparently higher over the mere Ni_3S_4 electrode (1.17–0.24 F cm^{-2}, 21% C_A retaining ratio within 0.62–18.6 mA cm^{-2}) and Co precursor electrode (2.80–0.90 F cm^{-2}, 32% C_A retaining ratio within 0.89–26.7 mA cm^{-2}). The enhanced rate capability is mainly attributed to the core-sheath heterostructure assembled by porous Co_3S_4 nanowire arrays and the intertwined porous Ni_3S_4 nanosheets network with vertical macroporous channels, the fast electrons/ions migration enable high C_As at increased current densities.

The cycleabilities of the three electrodes were measured by 5000 consecutive GCD cycles at similar current densities, from Fig. 5g, 81% of the initial C_A was maintained for Co_3S_4@Ni_3S_4 electrode undergoes 5000 GCD cycles at 8 mA cm^{-2}, which is apparently higher over the mere Ni_3S_4 electrode (57% initial C_A maintaining ratio at 6.2 mA cm^{-2}) and Co precursor electrodes (45% maintaining ratio at 8.9 mA cm^{-2}), showing the prominent cycleability. Fig. 5h shows the EISs of Co_3S_4@Ni_3S_4 electrode before and after 5000 GCD cycles, the R_s maintains unvaried whereas the R_{ct} increases slightly after GCD cycles, which reflects the gradual deactivation of the faradic sulfides. The morphology and phase of the Co_3S_4@Ni_3S_4 electrode after 5000 GCD cycles were also monitored, as shown in Fig. S7, the SEM image shows the stacked nanosheets with more dense texture (Fig. S7a), which reflects

the aggregation of Ni_3S_4 nanosheets during GCD cycles, the decrement in accessible surface area is one of the factors for the reduced C_A. Additionally, the diffractions belonging to Co_3S_4 and Ni_3S_4 are illegible (Fig. S7b), the amorphous phase suggests the lattice of the Co_3S_4 and Ni_3S_4 are gradually broken by the participation of OH^- ions during repeated GCD cycles, which is another possible factor reducing the C_A. In all, given the highest C_A, decent rate capability and cycleability, the Co_3S_4@Ni_3S_4 electrode is a credible faradic electrode for efficient supercapacitor.

3.3. Capacitive performance of the Co_3S_4@Ni_3S_4//PC HSC

To further evaluate the practical performance of the binder free Co_3S_4@Ni_3S_4 electrode in full-cell, a hybrid supercapacitor (HSC) was fabricated using the Co_3S_4@Ni_3S_4 electrode as positive electrode and PC electrode as negative electrode, which was labeled as Co_3S_4@Ni_3S_4//PC HSC. The PC electrode prepared by pyrolysis of carbon ink demonstrates EDL-feature within −0.1–0 V, the C_A gradually decreases from 0.27 to 0.13 F cm^{-2} within current density range of 1.1–22 mA cm^{-2}, and 64% of its initial C_A is maintained undergoes 5000 GCD cycles (Fig. S8), showing the feasibility as EDL-negative electrode. The active mass of PC electrode was tuned to 3 mg based on $m^+C_A{}^+V^+ = m^-C_A{}^-V^-$ to maximize the overall cell specific capacitance (C_{cell}). Fig. 6a shows the CVs of Co_3S_4@Ni_3S_4//PC HSC in different potential windows, the overall CV profiles include gradually increased anodic current and a wide cathodic peak. The broad and ambiguous redox peaks are mainly due to the less-defined partial voltage of positive electrode in 2-electrode system and the self-matching effect between the faradic positive and EDL-featured negative electrodes [48,49], the widening of faradic response causes the less legible redox peaks. With the extending of potential window from 0.6 to 1.6 V, the anodic current and cathodic peak intensity elevate progressively. As a consequence, the CV area enlarges drastically at wider voltage window, which means the prominently increased C_{cell} for the more pronounced faradic reactions of positive electrode at higher voltage range. Beyond 1.6 V, obvious anodic current attributable to oxygen evolution of electrolyte turns up, hence, 1.6 V is the optimal voltage window of the HSC.

Fig. 6b presents the GCDs of the HSC at different voltage windows, as observed, the discharge time elongates conspicuously with the gradual widening of voltage window, which means the substantially increased C_{cell} in wider voltage window. According to discharge time, the C_{cell}s are 0.03, 0.09, 0.17, 0.27 and 0.52 F cm^{-2}, respectively at 2 mA cm^{-2} within 0.8, 1.0, 1.2, 1.4 and 1.6 V, the substantially increased C_{cell} is mainly due to the more pronounced faradic reactions of positive electrode at wider voltage range, as evidenced by the higher capacitive currents and enlarged CV area at wider voltage window (Fig. 6a). The higher C_{cell} at wider voltage window is beneficial for dramatically increased energy density, further manifests that 1.6 V is the optimal voltage window for the HSC. Hence, detailed capacitive performances of the HSC at 1.6 V were further evaluated. Fig. 6c shows the CVs of the Co_3S_4@Ni_3S_4//PC HSC at different voltage scan rates, the capacitive current and CV loop area increase accordingly with voltage scan rate, the overall profile can be largely maintained even at 100 mV s^{-1} without severe distortion, manifesting the high electrons/ions conductivities of both electrodes, which are mainly relevant to the porous Co_3S_4@Ni_3S_4 heterostructure arrays with vertical electrons migration paths within the Co_3S_4 nanowire arrays and the vertically macroporous channels within the Ni_3S_4 network. Fig. 6d offers the GCDs of the Co_3S_4@Ni_3S_4//PC HSC at various current densities, all the curves demonstrate nonlinear charge-discharge profiles, the apparent difference from the faradic platform of positive electrode is mainly due to the coexistence of EDL-featured negative electrode in full cell. Moreover, the less legible IR of the device indicates the high conductivity of both electrode as a consequence of the vertical electrons/ions migration channels with short path lengths in positive electrode and the EDL-feature of the PC negative electrode. The C_{cell}s are 0.52, 0.43, 0.38, 0.32, 0.23, 0.13 and 0.11 F cm^{-2}, respectively, at 2, 4, 6, 10, 20, 40, 60 mA cm^{-2}, the 22% C_{cell} retaining ratio with 30 folds increased current density suggests that the HSC is more suitable for charge storage and delivery at lower operation current densities.

Areal Ragone plots of the Co_3S_4@Ni_3S_4//PC HSC was calculated and shown in Fig. 6e, the E_A is 0.19 mWh cm^{-2} at P_A of 1.72 mW cm^{-2}, and declines to 0.021 mWh cm^{-2} with P_A increases to 38.4 mW cm^{-2}, showing the good energy and power delivery abilities of the HSC. The E_A is lower than other sulfides and oxides based HSCs, such as $NiCo_2S_4$ nanotube array//rGO HSC (1.56 mWh cm^{-2} at 7.75 mW cm^{-2}) [50], Co_3S_4/NiO//PC HSC (0.64 mWh cm^{-2} at 3.2 mW cm^{-2}) [7], Cu(OH)$_2$@$Ni_2(OH)_2CO_3$//rGO HSC (0.28 mWh cm^{-2} at 25 mW cm^{-2}) [22]. Considering E_A depends heavily on the total amount of active materials onto both electrodes and the lightweight HSC herein, the E_A of Co_3S_4@Ni_3S_4//PC HSC is still acceptable. The E_A is higher over other asymmetric fibrous supercapacitors, such as NiO/Ni(OH)$_2$/PEDOT// ordered mesoporous carbon fiber supercapacitor (0.01 mWh cm^{-2} at 0.33 mW cm^{-2}) [51], PPy@MnO_2@rGO based yarn supercapacitor (0.01 mWh cm^{-2} at 0.01 mW cm^{-2}) [52] and CNT@Co_3S_4 composite based yarn supercapacitor (1 μWh cm^{-2} at 0.01 mW cm^{-2}) [53]. Fig. 6f summaries the volumetric Ragone plots of the Co_3S_4@Ni_3S_4//PC HSC, the E_V ranges within 0.95–0.11 mWh cm^{-3} with P_V increases from 8.6 to 192 mWh cm^{-3}, the E_V value is comparable to other chalcogenides based supercapacitors, including CuS//AC HSC (1.11 mWh cm^{-3}) [45] and $Ni_{0.34}Co_{0.66}Se_2$ based symmetric supercapacitor (0.73 mWh cm^{-3})

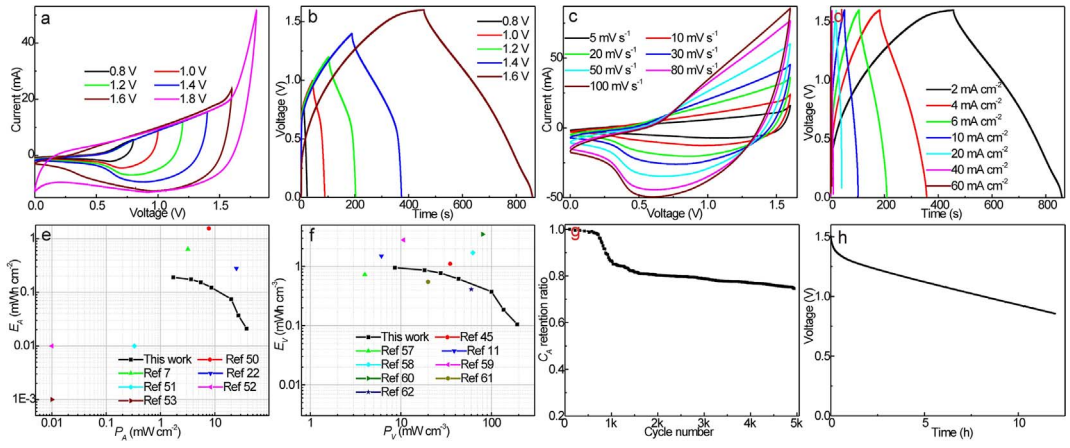

Fig. 6. (a) CVs at 10 mV s^{-1} within different voltage windows, (b) GCDs at 2 mA cm^{-2} within different voltage windows, (c) CVs at various voltage scan rates within 1.6 V, (d) GCDs at different current densities within 1.6 V, (e) Areal Ragone plots, (f) Volumetric Ragone plots, (g) Cycleability and (h) Open circuit voltage decay curve of the Co_3S_4@Ni_3S_4//PC HSC.

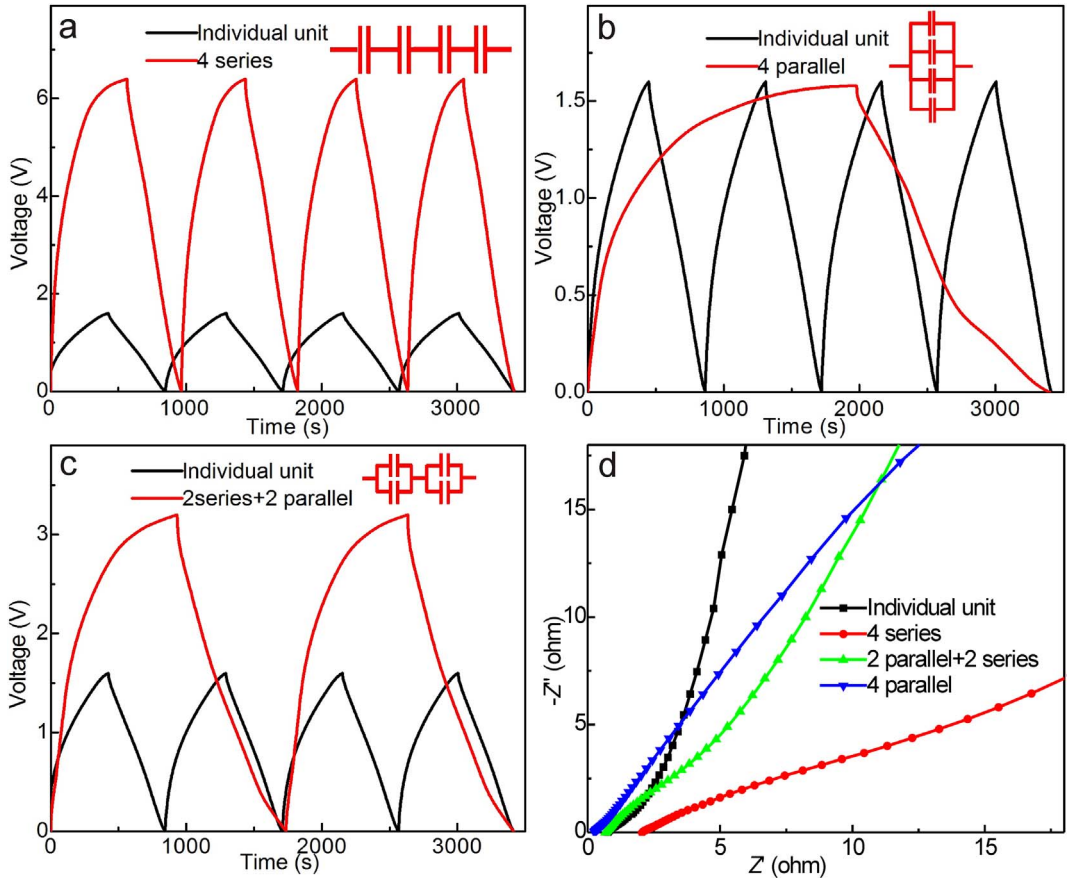

Fig. 7. GCD curves of 4-HSC arrays connected (a) in series, (b) in parallel, (c) in 2 series + 2 parallel. (d) EIS of the HSC arrays and individual HSC unit.

[57], slightly lower than Co_3O_4@Co_3S_4//AC HSC (1.5 mWh cm^{-3}) [11] and 3DHPC-$NiCo_2S_4$//3DHPC-Fe_2O_3 HSC (1.71 mWh cm^{-3}) [58], lower than the state-of-the-art devices such as $(NiCo)_{0.85}Se$//graphene HSC (2.85 mWh cm^{-3}) [59] and HP-CF@$NiCo_2S_4$//HP-CF@G-Fe_2O_3 HSC (3.55 mWh cm^{-3}) [60], whereas higher over other HSCs including MnO_2 nanowires//Fe_2O_3 nanotubes HSC (0.55 mWh cm^{-3}) [61] and MnO_2//Fe_2O_3 nanorods HSC (0.41 mWh cm^{-3}) [62]. In all, the considerable E_A and E_V of our HSC manifest the potential of the Co_3S_4@Ni_3S_4 heterostructure electrode in high performance HSC. Fig. 6g shows the cycleability of Co_3S_4@Ni_3S_4//PC HSC undergoes 5000 successive GCDs at 6 mA cm^{-2}, the C_{cell} maintains unvaried in the initial 700 cycles, which is mainly ascribable to the gradual wetting and activation of both electrodes in alkali medium. Subsequently, the C_{cell} decays gradually and finally maintains to be 78% after 5000 GCD cycles, showing the good cycleability of the HSC as a result of the good cycling abilities of both electrodes. In short, the high E_A, E_V and the good cycleability of our Co_3S_4@Ni_3S_4//PC HSC highlight the applicability of the binder free Co_3S_4@Ni_3S_4 heterostructure arrays electrode in efficient and long lifetime supercapacitor.

Fig. 6h presents the self-discharge behavior of the Co_3S_4@Ni_3S_4// PC HSC after being fully charged to 1.6 V at 2 mA cm^{-2} and subsequently shut the circuit. The HSC experiences fast voltage decay in the initial 1 h, and then levels off and finally retains to 0.85 V within 12 h, showing the good voltage retaining ability, the slow self-discharging behavior is mainly due to the battery-typed faradic feature of the positive electrode, the relatively slow redox kinetics slow down the self-discharging behavior. The self-discharge speed is faster than the symmetric supercapacitor based on two faradic $Ru_{0.58}In_{0.42}O{\cdot}nH_2O$/FMWCNTs electrode [54], comparable to graphene-Co_3O_4 based HSC [55], whereas obviously slower than EDL- featured carbonaceous symmetric supercapacitor [56], showing the effect of battery-typed faradic Co_3S_4@Ni_3S_4 electrode on the voltage retaining ability of HSC. Considering the fact that self-discharge is the main drawback of supercapacitor relative to batteries, the slow self-discharging is especially valuable for practical applications for the possibility of no need to immediately deliver the charges after being fully charged.

Although 1.6 V voltage window can be ensured in HSC, the voltage of an individual HSC still cannot satisfy the demand in operation voltage in practical applications. Therefore, the output parameters can be tuned by assembling individual HSC unit into supercapacitor arrays in different connecting manners. To evaluate the output performance of supercapacitor arrays, GCD curves of the HSC arrays by direct connection of 4 identical HSC units in series and/or in parallel configurations were evaluated. Fig. 7a compares the GCD curves of the 4-HSC array in series and individual unit at 2 mA cm^{-2}. In this 4-HSC array, the voltage is widened quadruply to 6.4 V, and the GCD curve exhibits similar charging-discharging time to individual unit with imperceptible IR, which indicates the good charge storage properties with low energy loss in the 4-HSC array. When 4 identical HSC units are connected in parallel and measured within the same voltage window (Fig. 7b), the discharging duration of the 4-HSC array is 4 times longer relative to the individual unit, indicating the total capacitance is 4 times higher than that of individual unit, which also attests the good capacitive performance in parallel assembly. The 4 identical supercapacitor units are further connected by assembling 2 units in parallel followed by linking the 2 sets of arrays in series (2 series + 2 parallel); the 4-HSC array shows doubled discharging duration under doubly enlarged voltage of 3.2 V (Fig. 7c). The almost equal total capacitance also indicates the good capacitance maintaining ability. The high capacitance retaining abilities in different arrays validate the feasibility of the Co_3S_4@Ni_3S_4// PC HSC in amplified supercapacitor arrays according to voltage and power output requirement in practical applications. EISs of the three

HSC arrays were compared with the individual HSC unit (Fig. 7d), all the devices demonstrate a low frequency straightline and a less legible arc at high frequency, the ill-defined R_{ct} arc is mainly due to the EDL-feature of the negative electrode in HSC, which depresses the faradic nature of positive electrode. The R_s value of the 4 array in series, 4 array in parallel and the 2 series + 2 parallel devices are 4, 0.25 and 1 times as the individual HSC unit, which conform to the general rationale in resistances of connected units. The order in resistances also proves the good charge storage abilities of the HSC arrays.

4. Conclusions

In summary, binder free Co_3S_4@Ni_3S_4 heterostructured arrays electrode was prepared by two step hydrothermal reactions using Ni foam as current collector and Ni source, and porous Co_3S_4 nanowire arrays serve as conductive backbone for the coating of intertwined Ni_3S_4 nanosheets to form heterostructure with vertically arranged macorporous channels and short electrons migration path length, therefore high C_A, decent rate capability and good cycleability of the electrode can be ensured. When used as positive electrode of full cell, the Co_3S_4@Ni_3S_4//PC HSC can deliver good energy delivery abilities and good cycleability, highlighting the potential of the porous Co_3S_4@Ni_3S_4 heterostructure arrays electrode in high performance and long lifetime energy storage device.

Conflicts of interests

There are no conflict to declare.

Acknowledgments

This work was supported by NSFC (Nos. 21671059 and 51772078), Program for Innovative Research Groups and Individuals in University of Henan Province (Nos. 18IRTSTHN002 and 15HASTIT006) and the 111 Project (No. D17007).

Appendix A. Supplementary data

Supplementary data associated with this article can be found, in the online version, at http://dx.doi.org/10.1016/j.cej.2018.03.042.

References

[1] Z.N. Yu, L. Tetard, L. Zhai, J. Thomas, Supercapacitor electrode materials: nanostructures from 0 to 3 dimensions, Energy Environ. Sci. 8 (2015) 702–730.
[2] L.L. Zhang, X.S. Zhao, Carbon-based materials as supercapacitor electrodes, Chem. Soc. Rev. 38 (2009) 2520–2531.
[3] Y.G. Wang, Y.F. Song, Y.Y. Xia, Electrochemical capacitors: mechanism, materials, systems, characterization and applications, Chem. Soc. Rev. 45 (2016) 5925–5950.
[4] Y.J. Ruan, C.D. Wang, J.J. Jiang, Nanostructured Ni compounds as electrode materials towards high-performance electrochemical capacitors, J. Mater. Chem. A 4 (2016) 14509–14538.
[5] L. Lv, K. Xu, C.D. Wang, H.Z. Wan, Y.J. Ruan, J. Liu, R.J. Zou, L. Miao, K. Ostrikov, Y.C. Lan, J.J. Jiang, Intercalation of glucose in NiMn-layered double hydroxide nanosheets: an effective path way towards battery-type electrodes with enhanced performance, Electrochim. Acta 216 (2016) 35–43.
[6] Y.F. Tian, Y.J. Ruan, J.Y. Zhang, Z.X. Yang, J.J. Jiang, C.D. Wang, Controllable growth of NiSe nanorod arrays via one-pot hydrothermal method for high areal-capacitance supercapacitors, Electrochim. Acta 250 (2017) 327–334.
[7] Y.H. Li, L.J. Cao, L. Qiao, M. Zhou, Y. Yang, P. Xiao, Y.H. Zhang, Ni-Co sulfide nanowires on nickel foam with ultrahigh capacitance for asymmetric supercapacitors, J. Mater. Chem. A 2 (2014) 6540–6548.
[8] X.H. Wang, H.Y. Xia, X.Q. Wang, B. Shi, Y. Fang, A super high performance asymmetric supercapacitor based on Co_3S_4/NiS nanoplates electrodes, RSC Adv. 6 (2016) 97482–97490.
[9] H.C. Chen, J.J. Jiang, L. Zhang, H.Z. Wan, T. Qi, D.D. Xia, Highly conductive $NiCo_2S_4$ urchin-like nanostructures for high-rate pseudocapacitors, Nanoscale 5 (2013) 8879–8883.
[10] Q.X. Chu, W. Wang, X.F. Wang, B. Yang, X.Y. Liu, J.H. Chen, Hierarchical $NiCo_2O_4$@nickel-sulfide nanoplate arrays for high performance supercapacitors, J. Power Sources 276 (2015) 19–25.
[11] B. Liu, D.Z. Kong, J. Zhang, Y. Wang, T.P. Chen, C.W. Cheng, H.Y. Yang, 3D hierarchical Co_3O_4@Co_3S_4 nanoarrays as cathode materials for asymmetric pseudocapacitors, J. Mater. Chem. A 4 (2016) 3287–3296.
[12] J. Wang, D.L. Chao, J.L. Liu, L.L. Li, L.F. Lai, J.Y. Lin, Z.X. Shen, Ni_3S_2@MoS_2 core/shell nanorod arrays on Ni foam for high-performance electrochemical energy storage, Nano Energy 7 (2014) 151–160.
[13] X.B. Liu, Z.P. Wu, Y.H. Yin, Hierarchical $NiCo_2S_4$@PANI core/shell nanowires grown on carbon fiber with enhanced electrochemical performance for hybrid supercapacitors, Chem. Eng. J. 323 (2017) 330–339.
[14] L.G. Beka, X. Li, W.H. Liu, Nickel cobalt sulfide core/shell structure on 3D Graphene for supercapacitor application, Sci. Rep. 7 (2017) 2105.
[15] X.H. Wang, B. Shi, Y. Fang, F. Rong, F.F. Huang, R.H. Que, M.W. Shao, High capacitance and rate capability of a Ni_3S_2@CdS core-shell nanostructure supercapacitor, J. Mater. Chem. A 5 (2017) 7165–7172.
[16] L.J. Cao, G. Tang, J. Mei, H. Liu, Construct hierarchical electrode with $Ni_xCo_{3-x}S_4$ nanosheet coated on $NiCo_2O_4$ nanowire arrays grown on carbon fiber paper for high-performance asymmetric supercapacitors, J. Power Sources 359 (2017) 262–269.
[17] X.J. Yang, L.J. Zhao, J.S. Lian, Arrays of hierarchical nickel sulfides/MoS_2 nanosheets supported on carbon nanotubes backbone as advanced anode materials for asymmetric supercapacitor, J. Power Sources 343 (2017) 373–382.
[18] J.H. Lin, Y.L. Liu, Y.H. Wang, H.N. Jia, S.L. Chen, J.L. Qi, C.Q. Qu, J. Cao, W.D. Fei, J.C. Feng, Rational construction of nickel cobalt sulfide nanoflakes on CoO nanosheets with the help of carbon layer as the battery-like electrode for supercapacitors, J. Power Sources 362 (2017) 64–72.
[19] H. Wang, C. Wang, C. Qing, D.M. Sun, B.X. Wang, G. Qu, M. Sun, Y.W. Tang, Construction of carbon-nickel cobalt sulphide hetero-structured arrays on nickel foam for high performance asymmetric supercapacitors, Electrochim. Acta 174 (2015) 1104–1112.
[20] H. Hua, S.J. Liu, Z.Y. Chen, R.Q. Bao, Y.Y. Shi, L.R. Hou, G. Pang, K.N. Hui, X.G. Zhang, C.Z. Yuan, Self-sacrifice template formation of hollow hetero-Ni_7S_6/Co_3S_4 nanoboxes with intriguing pseudocapacitance for high-performance electrochemical capacitors, Sci. Rep. 6 (2016) 20973.
[21] W.D. He, C.G. Wang, H.Q. Li, X.L. Deng, X.J. Xu, T.Y. Zhai, Ultrathin and porous Ni_3S_2/$CoNi_2S_4$ 3D-network structure for superhigh energy density asymmetric supercapacitors, Adv. Energy Mater. (2017) 1700983.
[22] S. Zhu, Z.D. Wang, F.Z. Huang, H. Zhang, S.K. Li, Hierarchical $Cu(OH)_2$@$Ni_2(OH)_2CO_3$ core/shell nanowire arrays in situ grown on three-dimensional copper foam for high-performance solid-state supercapacitors, J. Mater. Chem. A 5 (2017) 9960–9969.
[23] J.H. Lin, H.Y. Liang, H.N. Jia, S.L. Chen, J.L. Guo, J.L. Qi, C.Q. Qu, J. Cao, W.D. Fei, J.C. Feng, In situ encapsulated Fe_3O_4 nanosheet arrays with graphene layers as an anode for high-performance asymmetric supercapacitors, J. Mater. Chem. A 5 (2017) 24594–24601.
[24] Y. Zhang, W.P. Sun, X.H. Rui, B. Li, H.T. Tan, G.L. Guo, S. Madhavi, Y. Zong, Q.Y. Yan, One-pot synthesis of tunable crystalline Ni_3S_4@amorphous MoS_2 core/shell nanospheres for high-performance supercapacitors, Small 11 (2015) 3694–3702.
[25] X.J. Yang, H.M. Sun, P. Zan, L.J. Zhao, J.S. Lian, Growth of vertically aligned Co_3S_4/$CoMo_2S_4$ ultrathin nanosheets on reduced graphene oxide as a high-performance supercapacitor electrode, J. Mater. Chem. A 4 (2016) 18857–18867.
[26] L.N. Wang, J.J. Liu, L.L. Zhang, B.S. Dai, M. Xu, M.W. Ji, X.S. Zhao, C.B. Cao, J.T. Zhang, H.S. Zhu, Rigid three-dimensional Ni_3S_4 nanosheet frames: controlled synthesis and their enhanced electrochemical performance, RSC Adv. 5 (2015) 8422–8426.
[27] S.J. Patil, J.H. Kim, D.W. Lee, Graphene-nanosheet wrapped cobalt sulphide as a binder free hybrid electrode for asymmetric solid-state supercapacitor, J. Power Sources 342 (2017) 652–665.
[28] L. Liu, H. Rong, J.J. Li, X.W. Tong, Z.H. Wang, Synthesis of a hierarchical cobalt sulfide/cobalt basic salt nanocomposite via a vapor-phase hydrothermal method as an electrode material for supercapacitor, New J. Chem. 41 (2017) 12147–12152.
[29] S.G. Liu, C.P. Mao, Y.B. Niu, F.L. Yi, J.K. Hou, S.Y. Lu, J. Jiang, M.W. Xu, C.M. Li, Facile synthesis of novel networked ultralong cobalt sulfide nanotubes and its application in supercapacitors, ACS Appl. Mater. Interfaces 7 (2015) 25568–25573.
[30] L.R. Hou, Y.Y. Shi, S.Q. Zhu, M. Rehan, G. Pang, X.G. Zhang, C.Z. Yuan, Hollow mesoporous hetero-$NiCo_2S_4$/Co_9S_8 submicro-spindles: unusual formation and excellent pseudocapacitance towards hybrid supercapacitors, J. Mater. Chem. A 5 (2017) 133–144.
[31] C. Wei, Y. Huang, S.S. Xue, X. Zhang, X.F. Chen, J. Yan, W. Yao, One-step hydrothermal synthesis of flaky attached hollow-sphere structure $NiCo_2S_4$ for electrochemical capacitor application, Chem. Eng. J. 317 (2017) 873–881.
[32] S.J. Patil, J.H. Kim, D.W. Lee, Self-assembled Ni_3S_2//$CoNi_2S_4$ nanoarrays for ultra high-performance supercapacitor, Chem. Eng. J. 322 (2017) 498–509.
[33] T.T. Yang, R.Y. Li, Z.J. Li, Z.G. Gu, G.L. Wang, J.K. Liu, Hybrid of $NiCo_2S_4$ and nitrogen and sulphur-functionalized multiple graphene aerogel for application in supercapacitors and oxygen reduction with significant electrochemical synergy, Electrochim. Acta 211 (2016) 59–70.
[34] C. Marini, A. Perucchi, D. Chermisi, P. Dore, M. Valentini, D. Topwak, D.D. Sarma, S. Lupi, P. Postorino, Combined Raman and infrared investigation of the insulator-to-metal transition in $NiS_{2-x}Se_x$ compounds, Phys. Rev. B 84 (2011) 235134.
[35] Y.X. Xu, Z.Y. Lin, X.Q. Huang, Y. Wang, Y. Huang, X.F. Duan, Functionalized graphene hydrogel-based high-performance supercapacitors, Adv. Mater. 25 (2013) 5779–5784.
[36] J. Balamurugan, C. Li, T.D. Thanh, O.K. Park, N.H. Kim, J.H. Lee, Hierarchical design of $Cu_{1-x}Ni_xS$ nanosheets for high-performance asymmetric solid-state supercapacitors, J. Mater. Chem. A 5 (2017) 19760–19772.
[37] A. Mohammadi, N. Arsalani, A.G. Tabrizi, S.E. Moosavifard, Z. Naqshbandi,

L.S. Ghadimi, Engineering rGO-CNT wrapped Co_3S_4 nanocomposites for high-performance asymmetric supercapacitors, Chem. Eng. J. 334 (2018) 66–80.
[38] J.H. Lin, Y.L. Liu, Y.H. Wang, H.N. Jia, S.L. Chen, J.L. Qi, C.Q. Qu, J. Cao, W.D. Fei, J.C. Feng, Designed formation of NiO@C@Cu_2O hybrid arrays as battery-like electrode with enhanced electrochemical performances, Ceram. Int. 43 (2017) 15410–15417.
[39] J.H. Lin, H.Y. Liang, H.N. Jia, S.L. Chen, Y.F. Cai, J.L. Qi, J. Cao, W.D. Fei, J.C. Feng, Hierarchical $CuCo_2O_4$@$NiMoO_4$ core-shell hybrid arrays as the battery-like electrode for supercapacitors, Inorg. Chem. Front. 4 (2017) 1575–1581.
[40] J.H. Lin, H.N. Jia, H.Y. Liang, S.L. Chen, Y.F. Cai, J.L. Qi, C.Q. Qu, J. Cao, W.D. Fei, J.C. Feng, In situ synthesis of vertical standing nanosized NiO encapsulated in graphene as electrodes for high-performance supercapacitors, Adv. Sci. 1700687 (2017).
[41] M.L. Yan, Y.D. Yao, J.Q. Wen, L. Long, M.L. Kong, G.G. Zhang, X.M. Liao, G.F. Yin, Z.B. Huang, Construction of a hierarchical $NiCo_2S_4$@PPy core-shell heterostructure nanotube array on Ni foam for a high-performance asymmetric supercapacitor, ACS Appl. Mater. Interfaces 8 (2016) 24525–24535.
[42] X.J. Wei, X.Q. Jiang, J.S. Wei, S.Y. Gao, Functional groups and pore size distribution do matter to hierarchically porous carbons as high-rate-performance supercapacitors, Chem. Mater. 28 (2016) 445–458.
[43] H.N. Jia, J.H. Lin, Y.L. Liu, S.L. Chen, Y.F. Cai, J.L. Qi, J.C. Feng, W.D. Fei, Nanosized core-shell structured graphene-MnO_2 nanosheet arrays as stable electrodes for superior supercapacitors, J. Mater. Chem. A 5 (2017) 10678–10686.
[44] J.H. Lin, H.N. Jia, Y.F. Cai, S.L. Chen, H.Y. Liang, X. Wang, F. Zhang, J.L. Qi, J. Cao, J.C. Feng, W.D. Fei, Modifying the electrochemical performance of vertically-oriented few-layered graphene through rotary plasma processing, J. Mater. Chem. A 6 (2018) 908–917.
[45] Y.W. Lee, B.S. Kim, J. Hong, J.W. Lee, S.Y. Pak, H.S. Jang, D.M. Whang, S.N. Cha, J.I. Sohn, J.M. Kim, A pseudo-capacitive chalcogenide-based electrode with dense 1-dimensional nanoarrays for enhanced energy density in asymmetric supercapacitors, J. Mater. Chem. A 4 (2016) 10084–10090.
[46] X. Liu, B. You, X.Y. Yu, J. Chipman, Y.J. Sun, Electrochemical oxidation to construct a nickel sulfide/oxide heterostructure with improvement of capacitance, J. Mater. Chem. A 4 (2016) 11611–11615.
[47] J. Hong, Y.W. Lee, D. Ahn, S. Pak, J. Lee, A.R. Jang, S. Lee, B. Hou, Y. Cho, S.M. Morris, H.S. Shin, S.N. Cha, J.I. Sohn, J.M. Kim, Highly stable 3D porous heterostructures with hierarchically-coordinated octahedral transition metals for enhanced performance supercapacitors, Nano Energy 39 (2017) 337–345.
[48] N. An, Y.F. An, Z.A. Hu, B.S. Guo, Y.Y. Yang, Z.Q. Lei, Graphene hydrogels functionalized non-covalently by Alizarin: an ideal electrode materials for symmetric supercapacitor, J. Mater. Chem. A 3 (2015) 22239–22246.
[49] B.S. Guo, Z.A. Hu, Y.F. An, N. An, P.F. Jia, Y.D. Zhang, Y.Y. Yang, Z.M. Li, Nitrogen-doped heterostructure carbon functionalized by electroactive organic molecules for asymmetric supercapacitors with high energy density, RSC Adv. 6 (2016) 40602–40614.
[50] H.C. Chen, J.J. Jiang, L. Zhang, D.D. Xia, Y.D. Zhao, D.Q. Guo, T. Qi, H.Z. Wan, In situ growth of $NiCo_2S_4$ nanotube arrays on Ni foam for supercapacitors: Maximizing utilization efficiency at high mass loading to achieve ultrahigh areal pseudocapacitance, J. Power Sources 254 (2014) 249–257.
[51] H.L. Yang, H.H. Xu, M. Li, L. Zhang, Y.H. Huang, X.L. Hu, Assembly of NiO/Ni$(OH)_2$/PEDOT nanocomposites on contra wires for fiber-shaped flexible asymmetric supercapacitors, ACS Appl. Mater. Interfaces 8 (2016) 1774–1779.
[52] Y. Huang, H. Hu, Y. Huang, M.S. Zhu, W.J. Meng, C. Liu, Z.X. Pei, C.L. Hao, Z.K. Wang, C.L. Zhi, From industrially weavable and knittable highly conductive yarns to large wearable energy storage textiles, ACS Nano 9 (2015) 4766–4775.
[53] F.H. Su, X.M. Lv, M.H. Miao, High-performance two-ply yarn supercapacitors based on carbon nanotube yarns dotted with Co_3O_4 and NiO nanoparticles, Small 11 (2015) 854–861.
[54] C.Z. Yuan, L.R. Hou, L. Yang, D.K. Li, J. Tan, L.F. Shen, F. Zhang, X.G. Zhang, Synthesis of $Ru_{0.58}In_{0.42}O_y{\cdot}nH_2O$ nanoparticles dispersed onto poly(sodium-4-styrene sulfonate)-functionalized multi-walled carbon nanotubes and their application for electrochemical capacitors, J. Colloid Interface Sci. 354 (2011) 804–809.
[55] Z.Y. Gao, C. Chen, J.L. Chang, L.M. Chen, D.P. Wu, F. Xu, K. Jiang, Balanced energy density and power density: asymmetric supercapacitor based on activated fullerene carbon soot anode and graphene-Co_3O_4 composite cathode, Electrochim. Acta 260 (2018) 932–943.
[56] J.L. Chang, Z.Y. Gao, X. Liu, D.P. Wu, F. Xu, Y.W. Guo, Y.M. Guo, K. Jiang, Hierarchically porous carbons with graphene incorporation for efficient supercapacitors, Electrochim. Acta 213 (2016) 382–392.
[57] P. Xu, W. Zeng, S.H. Luo, C.X. Ling, J.W. Xiao, A.J. Zhou, Y.M. Sun, K. Liao, 3D Ni-Co selenide nanorod array grown on carbon fiber paper: towards high-performance flexible supercapacitor electrode with new energy storage mechanism, Electrochim. Acta 241 (2017) 41–49.
[58] H.L. Fan, W. Liu, W.Z. Shen, Honeycomb-like composite structure for advanced solid state asymmetric supercapacitors, Chem. Eng. J. 326 (2017) 518–527.
[59] C. Xia, Q. Jiang, C. Zhao, P.M. Beaujuge, H.N. Alshareef, Asymmetric supercapacitors with metal-like ternary selenides and porous graphene electrodes, Nano Energy 24 (2016) 78–86.
[60] J.Z. Chen, J.L. Xu, S. Zhou, N. Zhao, C.P. Wong, Nitrogen-doped hierarchically porous carbon foam: a free-standing electrode and mechanical support for high-performance supercapacitors, Nano Energy 25 (2016) 193–202.
[61] P.H. Yang, Y. Ding, Z.Y. Lin, Z.W. Chen, Y.Z. Li, P.F. Qiang, M. Ebrahimi, W.J. Mai, C.P. Wong, Z.L. Wang, Low-cost high-performance solid-state asymmetric supercapacitors based on MnO_2 nanowires and Fe_2o_3 nanotubes, Nano Lett. 14 (2014) 731–736.
[62] X.H. Lu, Y.X. Zeng, M.H. Yu, T. Zhai, C.L. Liang, S.L. Xie, M.S. Balogun, Y.X. Tong, Oxygen-deficient hematite nanorods as high-performance and novel negative electrodes for flexible asymmetric supercapacitors, Adv. Mater. 26 (2014) 3148–3155.